# Experimental platform for combining high pressure and swift heavy ion irradiations

Ioannis Tzifas,[1,*] Kay-Obbe Voss,[1] Christopher Schröck,[1,2] Pascal Simon,[1] Jiaxu Liang,[2] Lkhamsuren Bayarjargal,[2] Maik Lang,[3] Reinhard Boehler,[4] David Merges,[2] Leon Kirsch,[1] Emanuil Zeqo,[1,5] Bjoern Winkler,[2] Maria-Eugenia Toimil-Molares,[1,5,†] and Christina Trautmann[1]

[1]*GSI Helmholtzzentrum für Schwerionenforschung, 64291 Darmstadt, Germany*

[2]*Goethe Universität Frankfurt, 60438 Frankfurt, Germany*

[3]*University of Tennessee, Knoxville, Tennessee 37996, USA*

[4]*Neutron Scattering Division, Neutron Sciences Directorate, Oak Ridge National Laboratory, Oak Ridge, Tennessee 37830, USA*

[5]*Material- und Geowissenschaften, Technische Universität Darmstadt, 64287 Darmstadt, Germany*

(Received 15 January 2026; accepted 13 March 2026; published 16 April 2026)

This paper presents the technical details and commissioning results of a newly upgraded platform for ion-irradiation experiments under multi-GPa static pressure conditions at the GSI Helmholtz Center for Heavy Ion Research (Darmstadt, Germany), now accessible to external users. The GSI SIS18 accelerator provides heavy ions with tens of GeV kinetic energies, capable of penetrating through diamond anvil cells and depositing extremely high energy densities within the pressurized samples. This energy deposition triggers ultrafast, localized structural and phase transformations at the nanoscale. The platform integrates online optical microscopy and Raman spectroscopy, providing real-time monitoring of material modifications during stepwise fluence accumulation. By enabling controlled studies of structural responses and phase transitions under coupled extreme conditions, this setup opens unprecedented opportunities for research across condensed-matter physics, materials science, geoscience, high-pressure chemistry, and planetary science.

DOI: 10.1103/q8w6-wttf

## I. INTRODUCTION

The behavior of matter under extreme environments is a central topic across diverse research fields, including materials science, condensed-matter physics, extreme-conditions chemistry, geophysics, and planetary science [1–7]. Among the many forms of extreme conditions, the simultaneous application of high-dose ionizing radiation and pressure is particularly compelling, as it can fundamentally transform electronic structures, bonding characteristics, and defect dynamics. Understanding the interplay between high-energy ion irradiation and high static pressures provides unprecedented opportunities to uncover phenomena such as phase transitions, the formation of metastable high-pressure phases, and radiation-induced damage processes in functional materials and planetary interiors.

Here, we present a first-of-its-kind experimental platform that combines static high-pressure techniques with controlled exposure to relativistic heavy ions and integrated *in situ* diagnostics. The setup enables micrometer-sized samples compressed within diamond anvil cells (DACs) to be irradiated while being simultaneously monitored by *in situ* Raman spectroscopy and optical microscopy, allowing structural and optical changes to be tracked as a function of the accumulated radiation dose.

Before describing the design, capabilities, and commissioning results of this new station, we provide an overview of the key ion-matter interaction processes and summarize previous pioneering experimental approaches to ion-irradiation experiments under high pressure.

### A. Ion-matter interaction processes

Irradiation of materials with swift heavy ions of MeV to GeV kinetic energy creates unique extreme conditions as each ion deposits a huge amount of energy within a highly localized region on a subpicosecond timescale [8–11]. At these high kinetic energies, the incoming ions mainly transfer their energy to the electrons of the target material (electronic energy loss), causing strong electronic excitation and ionization. Along their path, each ion deposits several keV of energy per nanometer within a narrow cylindrical region only a few nanometers wide. This highly localized energy deposition corresponds to a few eV per atom, sufficient to break many atomic bonds and strongly disturb the local atomic structure.

The timescale of electronic and atomic processes determining the material response to an ion impact spans over many orders of magnitude. The initial electronic excitation and ionization occur almost instantaneously, producing energetic primary electrons within $10^{-17}$ to $10^{-15}$ s. This is followed by a cascade of secondary electrons that radially dissipate

*Contact author: i.tzifas@gsi.de

†Contact author: m.e.toimilmolares@gsi.de

*Published by the American Physical Society under the terms of the Creative Commons Attribution 4.0 International license. Further distribution of this work must maintain attribution to the author(s) and the published article's title, journal citation, and DOI.*

the energy over timescales of $10^{-15}$ to $10^{-13}$ s. During this stage, the atoms remain quasi-immobile until energy from the excited electron subsystem is transferred to the atomic lattice via electron-phonon coupling ($\sim 10^{-13}$ to $10^{-12}$ s), leading to a transient, highly localized lattice temperature rise that persists for $\sim 10^{-12}$ to $10^{-10}$ s and can initiate atomic motion and the formation of a cylindrical damage zone, commonly referred to as an ion track. Although ion-track formation has been studied for decades, the specific mechanisms driving structural modifications in the ion track remain a subject of intensive debate. Proposed processes include transient local melting, shock waves, rapid recrystallization, and the emission of secondary particles [10–12].

A widely used framework for describing track formation is the inelastic thermal spike model, which assumes that the rapid energy transfer from the electrons to the atoms results in a transient heat spike that melts a cylindrical zone around the ion trajectory within a few picoseconds. In this model, defect creation, microstructural changes, and amorphization in the track arise during the rapid cooling of the molten zone [13,14].

The creation of ion tracks requires electronic energy loss values above a material-specific threshold. The track diameters are typically between 5 and 10 nm while their length is set by the ion energy, extending from tens of micrometers for ions with specific energies around ~10 MeV per nucleon (MeV/u) to several mm for ions at ~200 MeV/u. The damage morphology of the tracks can differ significantly, ranging from continuous cylindrical damage to discontinuous defect fragments or irregular chains of defect clusters. Both track size and morphology are material specific and depend strongly on the energy loss of the projectile, which is a complex function of the ion's velocity and charge state [15].

The electronic energy loss $(dE/dx)_e$ can be calculated using the Bethe-Bloch formula [16]. It depends on the square of the ion's effective charge $Z_{\text{eff}}$, the ion velocity $v_p$ (which scales with the specific energy), and the atomic number of the target material $Z_t$:

$$\left(\frac{dE}{dx}\right)_e = \frac{4\pi e^4 (Z_{\text{eff}})^2 Z_t N_t}{m_e v_p^2} \times \left(\ln \frac{2m_e v_p^2}{I} \ln(1-\beta) - \beta^2\right),$$

where $N_t$ is the mass density of the target, $m_e$ the electron mass, $e$ the elementary charge, $I$ the ionization energy, and $\beta = v_p/c$ the projectile velocity with respect to the velocity of light $c$. The effective charge $Z_{\text{eff}}$ is the charge of the ion while traveling through matter. It depends primarily on the ion velocity and can change via electron capture and loss processes [17]. At relativistic velocities, the ions are nearly fully stripped ($Z_{\text{eff}}$ = nuclear charge $Z$), while at lower velocities the charge state is reduced ($Z_{\text{eff}} < Z$) [17].

To illustrate these dependencies, Fig. 1 shows the electronic energy loss curves of four different ion species as they slow down in a steel target over a large range of specific energies from 1 GeV/u down to 100 keV/u. Each curve exhibits a maximum, denoted as Bragg peak, at approximately 1–4 MeV/u, which corresponds to a remaining range of about 10–40 μm before the ions come to rest. Due to the quadratic

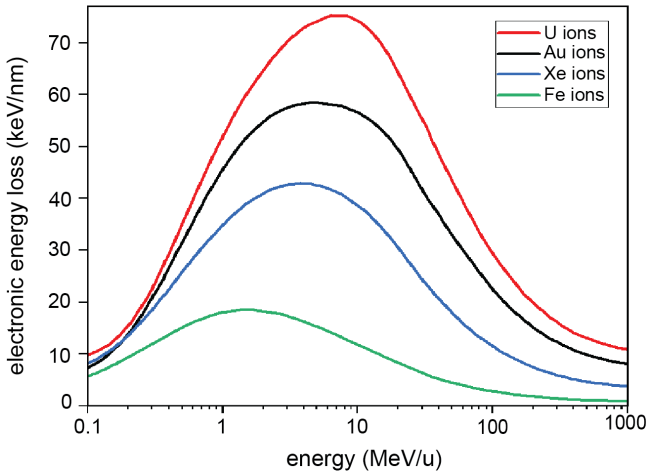


FIG. 1. Energy loss of high-energy ions as delivered by the SIS18 accelerator of GSI in stainless steel as a function of specific beam energy for various ion species (note the semilogarithmic scale).

dependence on $Z_{\text{eff}}$, the overall energy loss is largest for uranium ions, used for the commissioning of the platform, and decreases progressively for lighter ion species.

Most metallic materials and many semiconductors do not form tracks because their high electrical conductivity enables rapid dissipation of the deposited energy. In contrast, the best track recording materials are insulators, particularly those prone to amorphization, such as organic compounds, phosphates, silicates, oxides, and various ceramics [18–22]. A representative example of amorphous tracks within a crystalline ceramic matrix is shown in Fig. 2 [23,24]. Alkali and alkaline-earth halides tend to form chains of defect clusters along the ion path.

Some crystalline solids, including zirconia and certain sesquioxides, do not amorphize but undergo ion-induced crystalline-to-crystalline phase transitions [25,26]. A few oxides ($UO_2$, $ThO_2$, $CeO_2$, MgO, etc.) exhibit exceptional radiation resistance, responding only by forming isolated defects along the ion path [18–20].

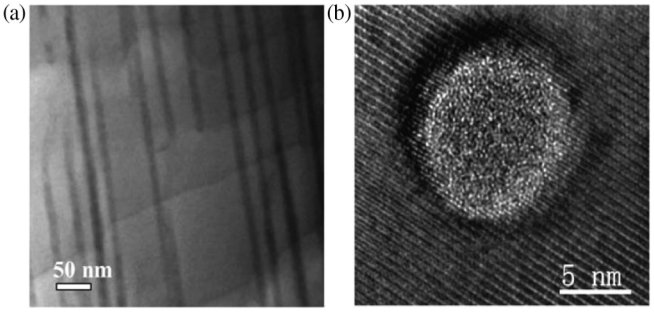


FIG. 2. Transmission electron microscopy images of amorphous ion tracks in $Gd_2Ti_2O_7$ pyrochlore irradiated under ambient conditions with 1.5 GeV U ions (6.3 MeV/u). (a) Highly parallel oriented tracks of few nanometers in diameter and several tens of micometers in length [23]. (b) Cross section of a single track embedded within the undamaged pyrochlore matrix, exhibiting a diameter of a few nanometers [24].

### B. Experimental background and prior work on ion irradiation under high pressure

Static high-pressure conditions can be conveniently generated using DACs. The attainable pressure range and sample dimensions are determined by the specific DAC design, especially the diamond geometrical properties and the preparation procedure (preindentation, drilled hole in gasket). Pressures in the range of a few to ∼300 GPa are routinely achievable, while reaching maximum pressures up to 1 TPa requires specialized DAC designs [27,28]. The transparency of the diamond anvils allows *in situ* characterization by a wide range of spectroscopic, optical, and diffraction techniques [29–35].

Combining ion irradiation with DAC-based systems, however, presents several experimental challenges. First, the ion energy must be sufficient for the ions to penetrate the pressurized sample and should ideally be tuned so that the energy loss peaks (Bragg maximum) within the sample volume. Second, beam collimation is essential to prevent coloration effects of the diamonds and unwanted activation of surrounding DAC components. Third, precise alignment of the DAC is mandatory to ensure the collimated beam hits the micrometer-sized target. Finally, *in situ* monitoring during irradiation is key for tracking structural and phase transformations as they occur, complementing conventional offline pre- and postirradiation characterization techniques.

In early approaches, ion irradiations were carried out by injecting the uncollimated relativistic heavy ions through the diamond anvil [36–44]. These experiments faced several limitations, including the formation of color centers that reduced the optical access through the diamonds and the lack of automated positioning and diagnostic tools, limiting the number of experiments achievable per beamtime campaign. Moreover, uncollimated beams activated the DACs and postirradiation characterization often required months for deactivation.

Despite these challenges, pioneering studies with relativistic swift heavy ions (e.g., Xe, Au, Pb, and U) demonstrated that the combined application of pressure and ion irradiation can trigger effects not observed under either condition alone. Notable examples comprise the following:

(1) Zircon ($ZrSiO_4$), a key mineral in fission-track geochronology, irradiated under simulated crustal conditions (750 MPa, 250 °C) exhibited slightly wider fission tracks than at ambient conditions, likely due to strain effects in the pressurized crystal lattice [44].

(2) High-pressure irradiation of zircon at tens of GPa (14 to 37 GPa) led to a decomposition into nanocrystals and the formation of reidite, a high-pressure polymorph typically found in meteorite impact sites. Predamaged natural zircon produced less reidite, indicating that the initial lattice defects influence phase transformations [43–45].

(3) High-pressure irradiation of pyrochlore ($Gd_2Zr_2O_7$) up to 40 GPa demonstrated a distinct pathway for stabilizing high-pressure phases to ambient conditions, a phase that is otherwise not accessible by conventional means [46,47].

(4) Similarly, zirconia ($ZrO_2$) under pressure (up to 11 GPa) and irradiation formed the orthorhombic-II phase far outside its normal stability field, a transformation that does not occur under pressure or irradiation alone [25,48]. The tetragonal phase generated at high pressures remained stable even upon decompression, demonstrating enhanced transformation efficiency under combined conditions.

The upgraded high-pressure irradiation platform is specifically designed to overcome the challenges outlined above. It features a remote-controlled beam collimation and alignment system for precise irradiation through the DAC gasket, while preserving optical access for *in situ* Raman spectroscopy and optical monitoring through the diamonds.

The combination of high pressure and swift heavy ion irradiation imposes several technical requirements:

(1) The sample size must be compatible with the specific high-pressure device, most commonly a DAC but also multi-anvil devices (e.g., Paris-Edinburgh press) can be used.

(2) The ions must have enough kinetic energy to penetrate and traverse the pressurized sample.

(3) The energy loss of the ions must be sufficiently large to induce detectable material modifications.

(4) The ion fluence (ions $cm^{-2}$) applied must be high enough to generate structural changes, observable via techniques such as x-ray diffraction, Raman spectroscopy, or transmission electron microscopy.

## II. ION BEAM FACILITY AND BEAM PARAMETER OPTIMIZATION

Relativistic heavy ions are provided by the heavy ion synchrotron SIS18 at the GSI Helmholtz Center in Darmstadt (Germany) (Fig. 3). A broad variety of ion species, from carbon to uranium, can be accelerated to energies ranging from 80 MeV/u up to 1 GeV/u, corresponding to velocities of up to ∼90% of the speed of light. The beam is initially accelerated by the Universal Linear Accelerator UNILAC and then injected into SIS18 at a specific energy of 11.4 MeV/u, with a typical pulse rate of ∼1 Hz. Beam parameters, including energy and intensity (ions per spill), can be precisely adjusted to meet specific experimental requirements.

After acceleration to the requested energy, the ion beam is extracted from SIS18 and guided through an evacuated beamline into Cave A. At the end of the beamline, the ions exit the vacuum through a thin metallic window and travel through several centimeters of air before entering the DAC.

For each experiment, the initial beam energy must be carefully adjusted to compensate for energy losses along the entire beam path. This includes losses from fixed components such as the ion-beam secondary electron transmission monitor (SEETRAM) (36 μm Ti), the 50 μm thick aluminum exit window, and an air gap of 30–50 cm. Beyond these in-beam components, the largest energy loss occurs within the DAC, depending on its geometry. The beam can pass either through the front diamond (for irradiation only, without *in situ* analysis) or through the gasket (Fig. 4).

To maximize radiation-induced effects, it is essential that the ions deposit the highest possible energy density into the sample. This is achieved by using heavy (high $Z$) ion species and irradiating the sample at energies close to the Bragg maximum (Fig. 5). A central challenge lies in accurately determining the path length through each DAC. Energy loss and range calculations are typically performed using simulation codes such as srim [49] or atima [50], which require various input parameters including thickness and density of

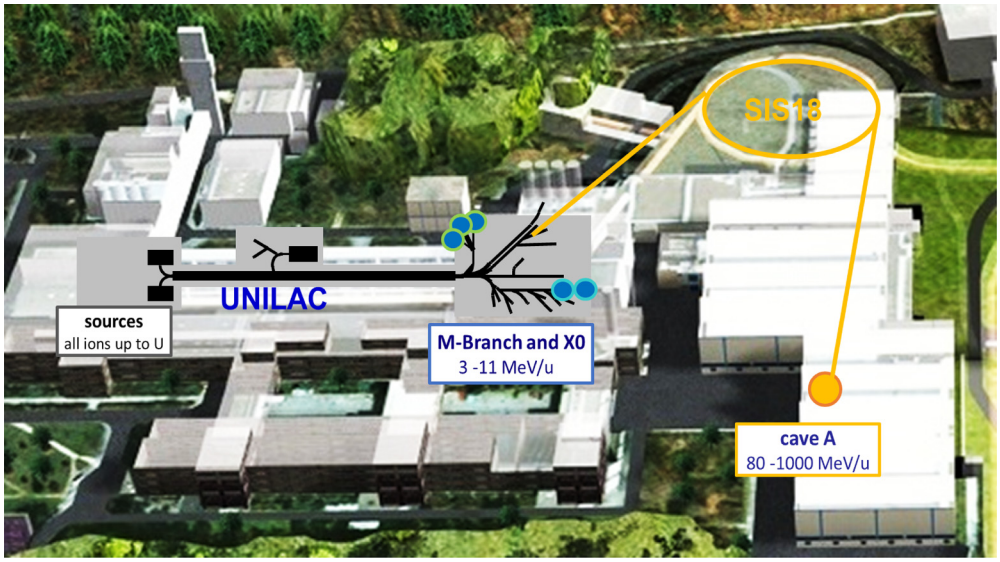


FIG. 3. Large-scale accelerator facility at the GSI Helmholtz Center for Heavy Ion Research in Darmstadt (Germany) providing all ion species up to relativistic specific energies (given in MeV per nucleon). The experimental station for high-pressure irradiations is located in Cave A. Further stations for materials research at UNILAC energies are located at M-branch and X0.

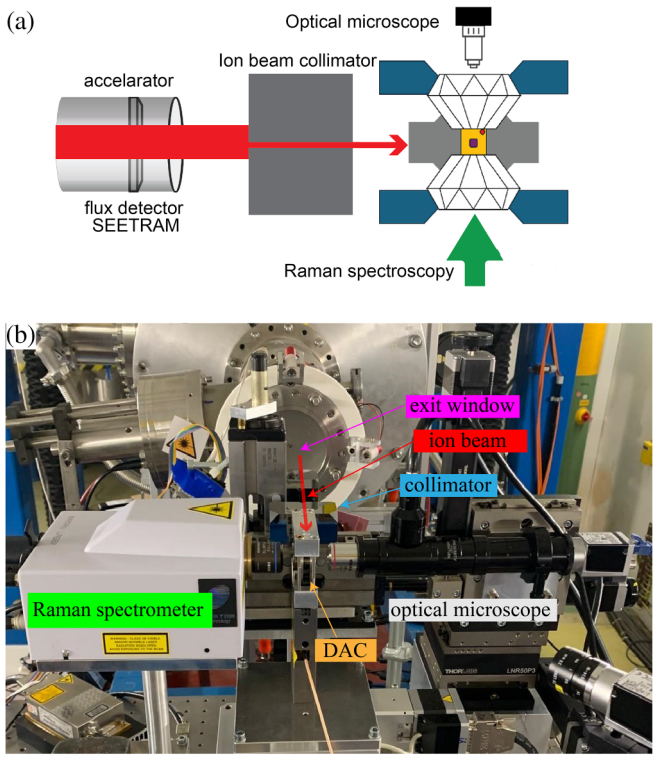


FIG. 4. Scheme [panel (a), not to scale] and photo [panel (b)] of the high-pressure irradiation platform in Cave A. The pulsed ion beam exits the vacuum beamline through an Al window, is collimated, and then passes through the gasket to penetrate the chamber containing the sample (purple) and the pressure gauge [usually a small ruby (red)]. This requires typically an initial ion energy in the range of 150–500 MeV/u depending on the material composition and size of the gasket. Beam-induced structural and optical changes in the samples are monitored *in situ* and in real time as a function of accumulated ion fluence.

all components along the beam path. These codes are based on the Bethe-Bloch formula in combination with interpolated experimental data and provide estimates for energy loss, ion range, and straggling values, taking into account the projectile energy, atomic number, and target density. Uncertainties particularly in the path length through the gasket can lead to cumulative errors of 10%–20% or more. Previous calibrations using well-defined diamond thicknesses, however, showed good agreement between the two codes, supporting their reliability under controlled conditions. Figure 5 illustrates an example of the energy loss as a function of the penetration depth for U ions with an initial energy of 250 MeV/u. After

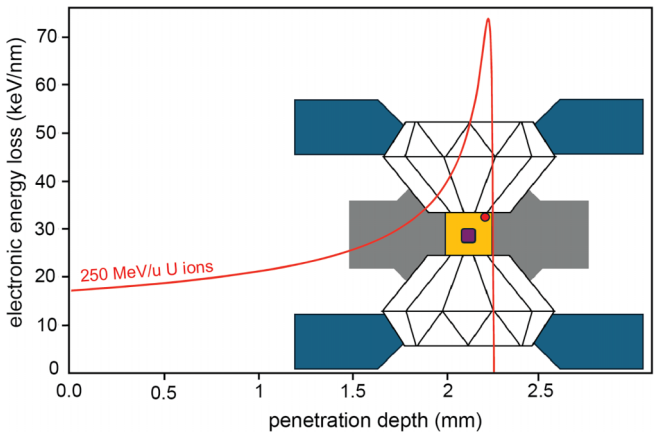


FIG. 5. Energy loss along the penetration depth (in red) when 250 MeV/u uranium ions enter the steel gasket of a DAC (not to scale) from the left. According to SRIM simulations [49], the U ions at this initial beam energy have a projected range of about 2.25 mm in the gasket. Ideally, the initial beam energy is chosen so that the Bragg maximum aligns with the sample volume (orange square). In this example, lower (higher) initial beam energies would shift the Bragg maximum toward the left (right).

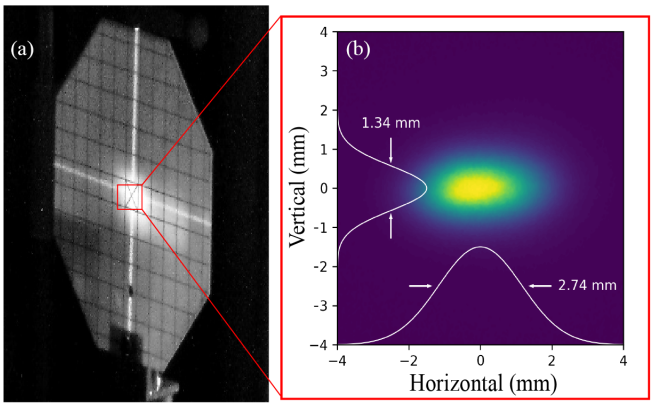


FIG. 6. (a) Video camera image of the uncollimated beam spot on a Chromox screen with a cm-scale raster. A calibrated laser system available in the cave provides horizontal and vertical reference lines, defining a cross-point that marks the nominal position of the ion beam. (b) Camera image of a representative, centered beam spot with approximate dimensions of 1.3 mm × 2.7 mm. Horizontal and vertical beam profiles are analyzed using a Python-based script.

traversing several beamline components, the ions experience their most significant deceleration within the steel gasket. The initial energy is chosen such that the Bragg peak occurs within the sample volume.

### A. Technical design and methods

#### *1. Ion beam control and diagnostics*

Due to the microscopic size of samples in DACs (usually 30–100 μm diameter), irradiation experiments require careful collimation and alignment procedures using dedicated beam diagnostics. Prior to the irradiation of the sample, the ion beam is focused to a spot of a few millimeters in diameter using large quadrupole magnets. A further reduction of the spot size is constrained by the beam's magnetic rigidity at relativistic velocities. The intensity of the primary beam is continuously monitored, pulse by pulse, with a SEETRAM detector (consisting of three thin titanium foils) installed inside the evacuated beamline upstream of the beam exit window [Fig. 4(a)]. Beam position and profile are visualized with a radiation-resistant scintillation screen (Chromox $Al_2O_3$:Cr) mounted on a flip holder in front of the collimator (Fig. 6).

To further reduce the beam size and prevent undesired irradiation of DAC components, we developed a collimation system with a remotely controlled, adjustable aperture. The system consists of two pairs of tungsten carbide cubes that fully intercept the primary beam. To ensure homogeneous exposure of the entire sample, we used a typical aperture size of 250 μm × 250 μm; however, the system can be adjusted to smaller or larger apertures ranging from few micrometers to millimeters to accommodate specific experimental requirements. Optimal beam transmission is achieved by fine-tuning the collimator's pitch ($\theta$) and yaw ($\phi$) angles until the ion-beam signal behind the aperture reaches its maximum.

The entire setup is controlled via a user-friendly software interface, which enables automated beamline control, collimation alignment, and fluence monitoring. Users can specify the desired fluence, and the system automatically stops the irradiation once the target value is reached. All extracted spills are logged automatically for record keeping and analysis.

For high-pressure irradiation experiments with heavy ions (e.g., Au or U), typical beam intensities range between $1 \times 10^8$ and $3 \times 10^9$ ions per spill, with a spill repetition of one spill every 1–3 s. The beam intensity is independent of beam energy and ion species. The irradiation of a DAC with a fluence of $1 \times 10^{12}$ ions cm$^{-2}$ may require 30–90 min, depending on the beam intensity. Even under extreme beam conditions (i.e., high energy loss and maximum pulse intensity), calculations indicate that the overall thermal load remains low due to the short pulse duration and low repetition rate, and a significant increase in sample temperature can be excluded.

The applied fluence is adjusted according to the sample sensitivity and the intended material modifications. As the fluence increases (e.g., from $10^9$ to $10^{13}$ ions cm$^{-2}$), the overall damage evolution progresses gradually from isolated single tracks to a track-overlapping regime, eventually resulting in complete track coverage of the material. The exact transition depends on the material-specific size of individual tracks that have a typically diameter between 5 and 10 nm.

To accurately determine the applied fluence at the sample position, postbeamtime cross-checks can be conducted using ion-track etching. For this, a thin polymer foil (e.g., 20–50 μm thick polycarbonate) is placed at the DAC position and exposed to a defined number of ion pulses. By wet chemical etching, each ion track is converted into a pore [11]. The ion fluence is quantified by counting the number of pores per unit area in the test foil using optical or scanning electron microscopy.

#### *2. fluka simulation of ion-beam fragmentation through the gasket*

While the accelerator provides an initially pure isotope beam, nuclear reactions in beamline components and in the DAC gasket can cause partial fragmentation. The most pronounced effects occur within the millimeter-thick gasket. The relevant nuclear processes can be modeled using the Monte Carlo simulation package fluka [51]. For example, a pure $^{238}$U beam at 290 MeV/u passing through a 2.5 mm thick steel gasket retains approximately 70%–75% of the primary $^{238}$U ions, while the remaining 30%–25% undergo nuclear reactions or scattering processes. The dominant channels involve the emission of neutrons, protons, and alpha particles (1–4 amu), as well as fragmentation into medium-mass nuclei, evident by the spectrum of isotopes slightly lighter than uranium in the 80–150 amu range (Fig. 7). Despite fragmentation, the deposited energy still predominantly (∼90%) originates from the surviving primary ions due to their higher mass and relative abundance.

#### *3. Online Raman spectroscopy*

To monitor ion-beam-induced modifications during irradiation, a Raman spectrometer is integrated into the high-pressure platform. Spectra are collected through the diamond anvils, enabling direct observation of structural changes under extreme conditions. The system includes a Horiba, iHR320 spectrometer (f/4.1) with a kinematic triple grating turret (800, 1200, 1800 l/mm) and is coupled to a

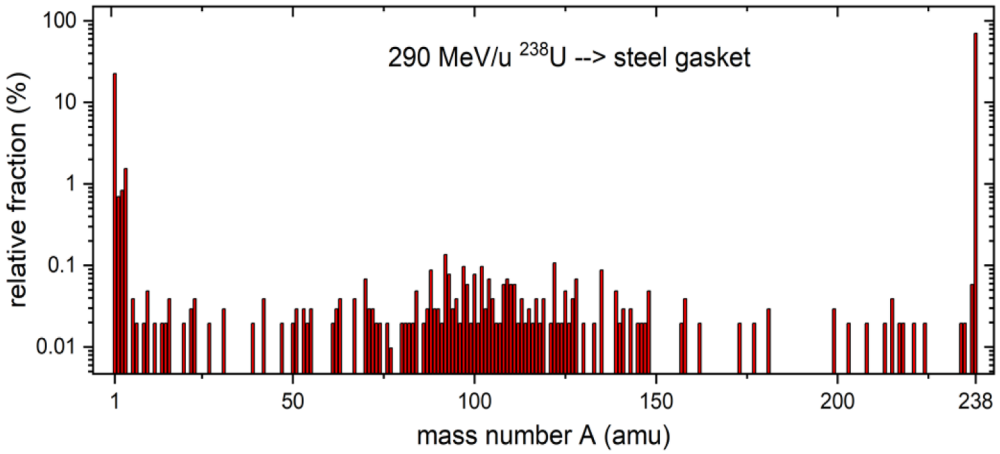


FIG. 7. fluka-simulated isotope histogram for 290 MeV/u U ions after passing through a 2.5 mm thick stainless steel gasket. Fractions are normalized to the total number of all particles leaving the gasket.

thermoelectrically cooled charge-coupled device (CCD) camera (−60 °C). The system is positioned behind a concrete wall to shield it from background radiation. The setup also includes a fiber optic probe with a low-noise green laser (100 mW, 532 nm). The spot size of the laser beam is about 2 $\mu m^2$. The spectrometer is equipped with a Syncerity 1024 × 256 detector yielding a spectral resolution of 0.1045 nm (FWHM), corresponding to a Raman resolution of approximately 3.3 $cm^{-1}$ at 532 nm excitation near 1000 $cm^{-1}$. Complementary to Raman spectroscopy, white-light illumination and a high-resolution color confocal camera enable precise visualization of both the sample and the laser spot during irradiation. Raman spectra can, in principle, be acquired during ion irradiation. However, simultaneous ion irradiation during the acquisition leads to a substantial increase in the spectral background, which significantly degrades the data quality and limits a reliable analysis. For this reason, our standard procedure is to interrupt the ion beam prior to Raman data acquisition. Depending on the spectral region of interest and signal intensity, the acquisition time for a single Raman spectrum is typically several minutes.

### B. First experimental findings and emerging research opportunities

The commissioning of the high-pressure irradiation platform marks a major milestone in our ability to investigate the interplay between high pressure and ion irradiation in real time. Extensive testing and optimization have demonstrated that the setup can reliably conduct irradiation experiments under controlled static high-pressure conditions. In the initial series of commissioning experiments, the ion fluence was increased stepwise, with *in situ* Raman spectra recorded during brief beam interruptions. These experiments demonstrate that the platform can be reliably employed to study ion-induced structural modifications under high pressure, with *in situ* monitoring via Raman spectroscopy. The irradiation included samples from various material classes: (1) the organic compound benzene ($C_6H_6$), (2) the inorganic compounds gadolinium oxide ($Gd_2O_3$) and sodium azide ($NaN_3$), and (3) bismuth (Bi) nanowires.

Irradiation of molecular systems can induce transitions from molecular states to extended atomic networks [52,53]. Figure 8 shows a series of Raman spectra of benzene at 10.0 GPa recorded before and after irradiation. At this pressure, benzene exists as a molecular solid with a relatively low melting point and weak intermolecular bonding. With stepwise increases in fluence from $1 \times 10^{12}$ to $3 \times 10^{13}$ ions $cm^{-2}$, the fluorescence background rises progressively, while the background-subtracted intensity of the $C_6H_6$ modes gradually decreases. At the highest fluence, when ion tracks fully cover the sample, all Raman peaks disappear. This is tentatively attributed to a complete structural transformation of the benzene, which requires confirmation by synchrotron x-ray diffraction measurements. Corresponding optical images show a color shift from its typical colorless state to a distinct orange-red color.

Another study focused on inorganic solids and their transformation between different polymorphs or states under extreme conditions. This is relevant, for example, to mimicking geological processes, synthesizing functional materials such as superconducting or superhard materials, and understanding the behavior and transformation pathways of functional materials [54]. During the first beamtime campaign, we irradiated $Gd_2O_3$ and $NaN_3$ samples compressed to 5.8 GPa with 240 and 200 MeV/u U ions, respectively. In the case of $Gd_2O_3$ and related oxides, understanding phase transformations and/or stabilization, defect accumulation, and irradiation-induced amorphization under combined pressure and irradiation conditions is highly relevant for nuclear technologies. In contrast, ion irradiation of $NaN_3$ under high pressure provides a unique opportunity to probe alternative chemical pathways in nitrogen-rich systems and may enable the exploration of polymeric or otherwise unconventional nitrogen phases that are inaccessible under ambient conditions.

The Raman spectra of $Gd_2O_3$ using Ne as pressure medium [Fig. 9(a)] reveal a gradual phase transformation with increasing ion fluence; however, the transformation remains incomplete even at the highest fluence of $1 \times 10^{12}$ ions $cm^{-2}$. In comparison, the Raman spectra of $NaN_3$ loaded with sodium chloride as pressure medium [Fig. 9(b)] indicate the

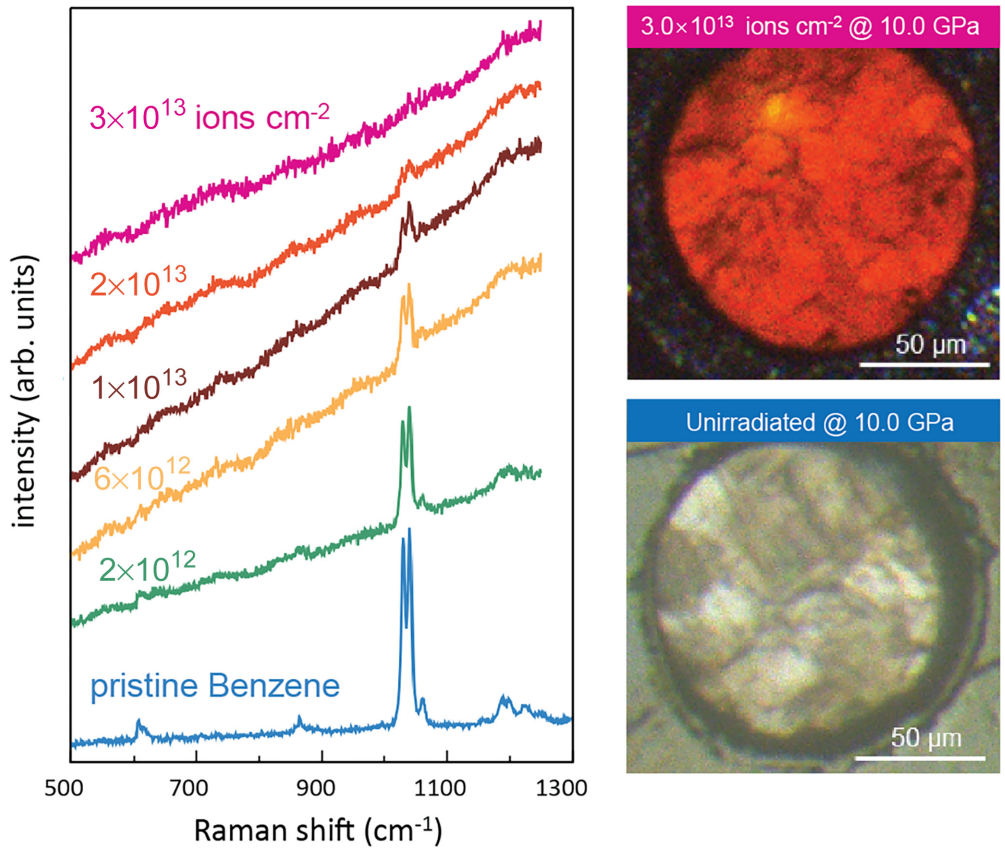


FIG. 8. Raman spectra recorded *in situ* during irradiation (235 MeV/u Au ions) with stepwise increase of the fluence for benzene pressurized at 10.0 GPa. The corresponding optical microscope images of the sample chamber reveal a clear transformation from the initially transparent (unirradiated) to a strongly colored sample (irradiated).

formation of a new phase with the original phase almost completely disappearing at a high fluence of $6 \times 10^{12}$ ions $cm^{-2}$.

These results demonstrate the capability of our platform to monitor the progression of phase transitions in a controlled manner and, if intended, to stop the irradiation at

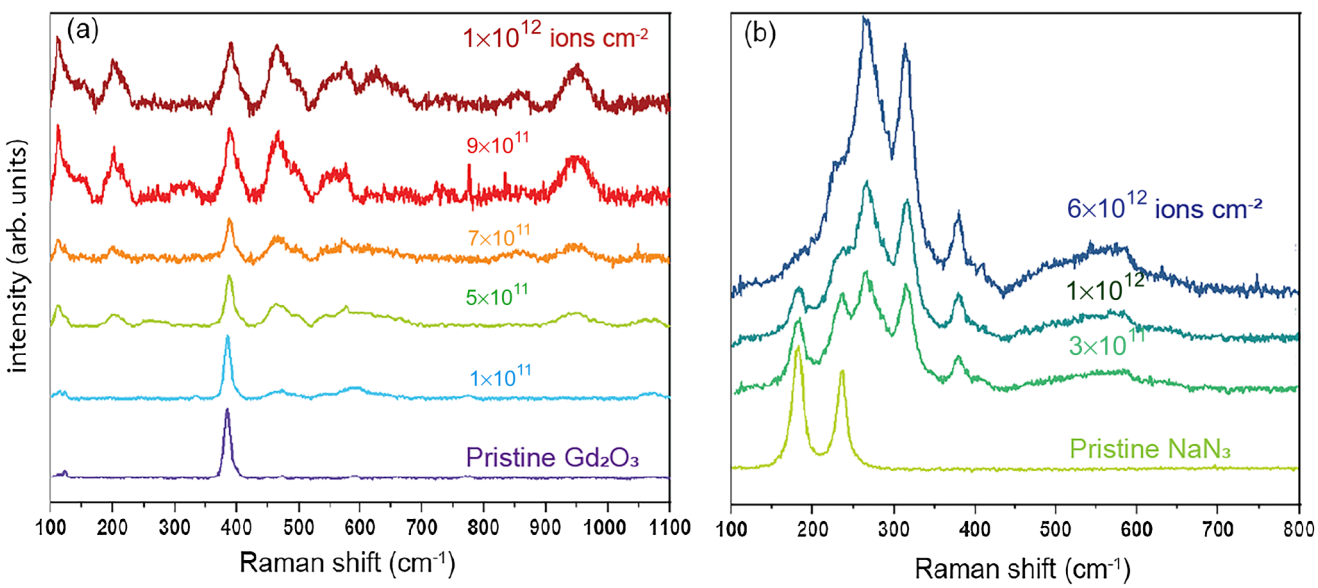


FIG. 9. Raman spectra recorded *in situ* during irradiation with stepwise increase of fluence. (a) $Gd_2O_3$ at 5.8 GPa (240 MeV/u U ions) and (b) $NaN_3$ at 5.8 GPa (200 MeV/u U ions).

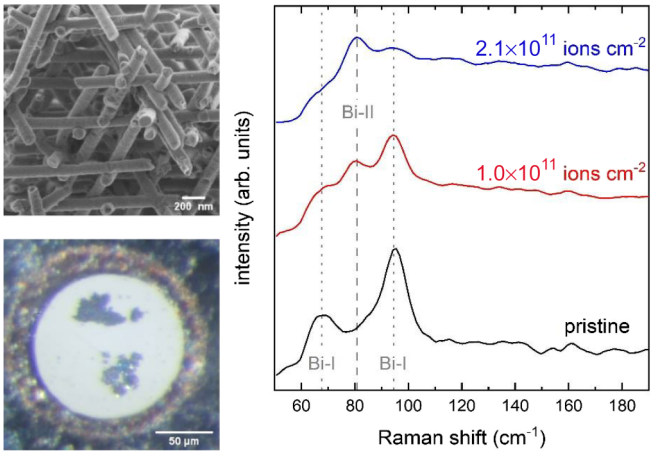


FIG. 10. (Left) SEM image of Bi-nanowire networks fabricated by ion-track technology [55] and optical image of gasket aperture loaded with the nanowire network and a microsized reference material. The hydrostatic pressure was 2.4 GPa using Ne as pressure medium. The irradiation was carried out with U ions of ∼30 MeV/u energy at the sample position. (Right) Raman spectra of nanowires exposed to various ion fluences.

intermediate transformation states. The different fluence dependence of $Gd_2O_3$ and $NaN_3$ demonstrates the ability of the setup to assess the radiation sensitivity of different materials by determining the fluence required to induce partial or complete phase transformations.

In addition to bulk and micrometer-sized samples, nanomaterials are of particular interest in high-pressure research because their stability fields can deviate substantially from bulk behavior. Nanomaterials often exhibit shifted transition pressures and distinct crystallographic transformation routes driven by geometry and size effects [55–58]. The combination of ion-beam-induced modifications and pressure effects offers promising opportunities for creating, stabilizing, and recovering previously inaccessible phases through precise control of the nanostructure dimensions. Figure 10 presents Raman spectra recorded during the irradiation of bismuth nanowires at 2.4 GPa, revealing a clear transition from the Bi-I to the Bi-II phase at a relatively low fluence of $1 \times 10^{11}$ ions cm$^{-2}$. To unambiguously identify the induced phases, future investigations will involve x-ray diffraction and transmission electron microscopy. Also, a systematic variation of the nanowire diameter, together with a direct comparison to bulk bismuth irradiated under identical ion-beam and pressure conditions, will be essential.

## III. CONCLUSIONS

The diverse results reported above highlight the novelty and promise of this experimental approach, as it enables direct monitoring of phase transformations as they occur and evolve under ion irradiation.

The central aspect of our approach is the extremely high energy density deposited by the ions, which generates intense electronic excitations and ultrafast thermal spikes capable of locally raising temperatures well beyond melting on timescales unattainable with conventional photon-based sources. This constitutes a unique route to drive the formation and stabilization of metastable phases; yet the underlying mechanisms, especially the role of irradiation-induced defects, remain to be fully uncovered.

Beyond enabling new discoveries, the platform provides an essential tool for validating theoretical models of defect behavior and phase stability under highly nonequilibrium, high-energy-density conditions. Together, these capabilities establish a foundation for a more comprehensive understanding of coupled thermodynamic and kinetic mechanisms that govern materials far from equilibrium.

In summary, this platform represents a significant leap forward in the exploration of matter under extreme conditions. It opens alternative avenues not only for discovering previously uncharacterized materials and phases, but also for their controlled engineering with implications for both fundamental and applied high pressure and materials science.

## IV. FOOTNOTE: ACCELERATOR ACCESS STATEMENT

Beamtime at the GSI facility and access to the new high-pressure platform are available to external users through a proposal-based system with evaluation by an independent review panel. For approved irradiation experiments, users can have access to the local infrastructure (including e.g., gasket preparation and a gas loading system) along with technical support. Further information can be obtained from the corresponding authors and via the GSI website [59].

## ACKNOWLEDGMENTS

The results presented here are based on experiments performed at the SIS18 at the GSI Helmholtzzentrum für Schwerionenforschung, Darmstadt (Germany) in the frame of FAIR Phase-0. Funding was generously provided by the BMBF in the framework of Projects No. 05K22RF3 and No. 05K25RF3 to Professor B.W. and the Goethe University. J.L. thanks the BMBF for funding his position. Part of the infrastructure for the DAC experiments was provided by funding from the Deutsche Forschungsgemeinschaft to B.W. (WI1232) and L.B. (BA4020). C.S. acknowledges funding via the R&D program of GSI and support from the Helmholtz Graduate School HGS-HIRe. M.L. acknowledges support from the U.S. Department of Energy-National Nuclear Security Administration (DOE-NNSA) under cooperative agreement DE-NA-0004153 (Chicago/DOE Alliance Center, CDAC). M.E.T-M and C.S. acknowledge support by the Helmholtz Innovation Pool Project MATHIPE.

The authors have no conflicts to disclose.

## DATA AVAILABILITY

The data that support the findings of this article are not publicly available. The data are available from the authors upon reasonable request.

[1] R. J. Hemley and W. Percy, Bridgman's second century, High Press. Res. **30**, 581 (2010).

[2] R. J. Hemley, Effects of high pressure on molecules, Annu. Rev. Phys. Chem. **51**, 763 (2000).

[3] H.-K. Mao, B. Chen, J. Chen, K. Li, J.-F. Lin, W. Yang, and H. Zheng, Recent advances in high-pressure science and technology, Matter Radiat. Extremes **1**, 59 (2016).

[4] C.-S. Yoo, Chemistry under extreme conditions: Pressure evolution of chemical bonding and structure in dense solids, Matter Radiat. Extremes **5**, 018202 (2020).

[5] Y. Song, W. Luo, Y. Wang, and C. Jin, Unveiling the enigma of matter under extreme conditions: From planetary cores to functional materials, Sci. Rep. **13**, 18340 (2023).

[6] J. L. Silva, A. C. Oliveira, T. C. R. G. Vieira, G. A. P. de Oliveira, M. C. Suarez, and D. Foguel, High-pressure chemical biology and biotechnology, Chem. Rev. **114**, 7239 (2014).

[7] L. Zhang, Y. Wang, J. Lv, and Y. Ma, Materials discovery at high pressures, Nat. Rev. Mater. **2**, 17005 (2017).

[8] M. Lang, R. Devanathan, M. Toulemonde, and C. Trautmann, Advances in understanding of swift heavy-ion tracks in complex ceramics, Curr. Opin. Solid State Mater. Sci. **19**, 39 (2015).

[9] M. Lang, F. Djurabekova, N. Medvedev, M. Toulemonde, and C. Trautmann, 1.15: Fundamental phenomena and applications of swift heavy ion irradiations, Compr. Nucl. Mater. **1**, 485 (2020).

[10] N. Medvedev, A. E. Volkov, R. Rymzhanov, F. Akhmetov, S. Gorbunov, R. Voronkov, and P. Babaev, Frontiers, challenges, and solutions in modeling of swift heavy ion effects in materials, J. Appl. Phys. **133**, 100701 (2023).

[11] C. Trautmann, Micro- and nanoengineering with ion tracks, in *Ion Beams in Nanoscience and Technology*, edited by R. Hellborg, H. J. Whitlow, and Y. Zhang (Springer, Berlin, 2009), pp. 369–387.

[12] R. A. Rymzhanov, N. Medvedev, J. H. O'Connell, V. A. Skuratov, A. Janse van Vuuren, S. A. Gorbunov, and A. E. Volkov, Insights into different stages of formation of swift heavy ion tracks, Nucl. Instrum. Methods Phys. Res. Sect. B **473**, 27 (2020).

[13] M. Toulemonde, C. Dufour, Z. Wang, and E. Paumier, Atomic and cluster ion bombardment in the electronic stopping power regime: A thermal spike description, Nucl. Instrum. Methods Phys. Res. B **112**, 26 (1996).

[14] M. Toulemonde, W. Assmann, C. Dufour, A. Meftah, and C. Trautmann, Nanometric transformation of matter by short and intense electronic excitation: Experimental data versus inelastic thermal spike model, Nucl. Instrum. Methods Phys. Res. B **277**, 28 (2012).

[15] M. Toulemonde, W. Assmann, C. Dufour, A. Meftah, F. Studer, and C. Trautmann, Experimental phenomena and thermal spike model description of ion tracks in amorphisable inorganic insulators, in *Ion Beam Science: Solved and Unsolved Problems*, Invited Lectures Presented at a Symposium in Copenhagen, 1–5 May 2006, edited by P. Sigmund (The Royal Danish Academy of Science and Letters, Copenhagen, 2006), Part I, p. 376.

[16] P. Sigmund, *Particle Penetration and Radiation Effects* (Springer, Berlin, Heidelberg, 2006).

[17] F. Hubert, R. Bimbot, and H. Gauvin, Semi-empirical formula for the effective charge of heavy ions in matter, At. Data Nucl. Data Tables **46**, 1 (1990).

[18] C. L. Tracy, M. Lang, F. Zhang, C. Trautmann, and R. C. Ewing, Phase transformations in $Ln_2O_3$ materials irradiated with swift heavy ions, Phys. Rev. B **92**, 174101 (2015).

[19] W. F. Cureton, R. I. Palomares, C. L. Tracy, E. C. O'Quinn, J. Walters, M. Zdorovets, R. C. Ewing, M. Toulemonde, and M. Lang, Effects of irradiation temperature on the response of $CeO_2$, $ThO_2$, and $UO_2$ to highly ionizing radiation, J. Nucl. Mater. **525**, 83 (2019).

[20] E. C. O'Quinn, C. L. Tracy, W. F. Cureton, R. Sachan, J. C. Neuefeind, C. Trautmannef, and M. K. Lang, Multi-scale investigation of heterogeneous swift heavy ion tracks in stannate pyrochlore, J. Mater. Chem. A **9**, 16982 (2021).

[21] C. Overstreet, J. Cooper, E. C. O'Quinn, W. F. Cureton, R. Palomares, J. Leys, G. Deissmann, S. Neumeier, C.-H. Chen, and M. K. Lang, Structural stability of REE-$PO_4$ (REE = Sm, Tb) under swift heavy ion irradiation, Nucl. Instrum. Methods Phys. Res. B **527**, 34 (2022).

[22] B. Afra, M. D. Rodriguez, C. Trautmann, O. H. Pakarinen, F. Djurabekova, K. Nordlund, T. Bierschenk, R. Giulian, M. C. Ridgway, G. Rizza, N. Kirby, M. Toulemonde, and P. Kluth, SAXS investigations of the morphology of swift heavy ion tracks in $\alpha$-quartz, J. Phys.: Condens. Matter **25**, 045006 (2013).

[23] J. Zhang, M. Toulemonde, M. Lang, J. M. Costantini, S. Della-Negra, and R. C. Ewing, $C_{60}$ and U ion irradiation of $Gd_2Ti_3Zr_{2-x}O_7$ pyrochlore, J. Mater. Res. **30**, 2456 (2015).

[24] J. M. Zhang, M. Lang, R. C. Ewing, R. Devanathan, W. J. Weber, and M. Toulemonde, Nanoscale phase transitions under extreme conditions within an ion track, J. Mater. Res. **25**, 1344 (2010).

[25] B. Schuster, M. Lang, R. Klein, C. Trautmann, R. Neumann, and A. Benyagoub, Structural phase transition in $ZrO_2$ induced by swift heavy ion irradiation at high pressure, Nucl. Instrum. Methods Phys. Res. B **267**, 964 (2009).

[26] A. P. Solomon, E. C. O'Quinn, J. Liu, I. M. Gussev, X. Guo, J. Neuefeind, C. Trautmann, R. C. Ewing, G. Baldinozzi, and M. K. Lang, Atomic-scale structure of $ZrO_2$: Formation of metastable polymorphs, Sci. Adv. **11**, eadq5943 (2025).

[27] L. Dubrovinsky, N. Dubrovinskaia, V. B. Prakapenka, and A. M. Abakumov, Implementation of micro-ball nanodiamond anvils for high-pressure studies above 6 Mbar, Nat. Commun. **3**, 1163 (2012).

[28] N. Dubrovinskaia, L. Dubrovinsky, N. A. Solopova, A. Abakumov, S. Turner, M. Hanfland, E. Bykova, M. Bykov, C. Prescher, V. B. Prakapenka, S. Petitgirard, I. Chuvashova, B. Gasharova, Y.-L. Mathis, P. Ershov, I. Snigireva, and A. Snigirev, Terapascal static pressure generation with ultrahigh yield strength nanodiamond, Sci. Adv. **2**, e1600341 (2016).

[29] H.-P. Liermann, Z. Konôpková, W. Morgenroth, K. Glazyrin, J. Bednarčik, E. E. McBride, S. Petitgirard, J. T. Delitz, M. Wendt, Y. Bican, A. Ehnes, I. Schwark, A. Rothkirch, M. Tischer, J. Heuer, H. Schulte-Schrepping, T. Krachta, and H. Franz, The extreme conditions beamline P02.2 and the extreme conditions science infrastructure at PETRA III, J. Synchrotron Radiat. **22**, 908 (2015).

[30] W. A. Bassett, Diamond anvil cell, 50th birthday, High Pressure Res. **29**, 163 (2009).

[31] X. Lu, S. Gao, P. Wu, Z. Zhang, L. Zhang, X. Li, and X. Qin, *In situ* high-pressure Raman spectroscopic, single-crystal X-ray diffraction, and FTIR investigations of rutile and $TiO_2$-II, Minerals **13**, 703 (2023).

[32] M. Bull, R. Huber, P. Yu, T. Finney, N. Felvey, P. Chow, Y. Xiao, T. Kuhl, and E. Watkins, *In-situ* SAXS and XRD of SBA-15 in a diamond anvil cell during high-pressure densification, Mendeley Data, V1 (2024), doi:10.17632/4sncvxbn6x.

[33] B. Haberl, M. Guthrie, and R. Boehler, Advancing neutron diffraction for accurate structural measurement of light elements at megabar pressures, Sci. Rep. **13**, 4741 (2023).

[34] R. Boehler, M. Guthrie, J. J. Molaison, A. M. dos Santos, S. Sinogeikin, S. Machida, N. Pradhan, and C. A. Tulk, Large-volume diamond cells for neutron diffraction above 90 GPa, High Pressure Res. **33**, 546 (2013).

[35] T. Meier, A. Aslandukova, F. Trybel, D. Laniel, T. Ishii, S. Khandarkhaeva, N. Dubrovinskaia, and L. Dubrovinsky, *In situ* high-pressure nuclear magnetic resonance crystallography in one and two dimensions, Matter Radiat. Extremes **6**, 068402 (2021).

[36] D. Schauries, B. Afra, P. Mota-Santiago, C. Trautmann, M. K. Lang, R. C. Ewing, N. Kirby, and P. Kluth, Annealing of ion tracks in apatite under pressure characterized *in situ* by small-angle x-ray scattering, Sci. Rep. **10**, 1367 (2020).

[37] B. Afra, K. Nordlund, M. D. Rodriguez, T. Bierschenk, C. Trautmann, S. Mudie, and P. Kluth, Thermal response of nanoscale cylindrical inclusions of amorphous silica embedded in $\alpha$-quartz, Phys. Rev. B **90**, 224108 (2014).

[38] M. K. Lang, The effect of pressure on ion track formation in minerals, doctoral dissertation, University of Heidelberg, 2004.

[39] M. Lang, U. A. Glasmacher, R. Neumann, D. Schardt, C. Trautmann, and G. A. Wagner, Energy loss of 50-GeV uranium ions in natural diamond, Appl. Phys. A **80**, 691 (2005).

[40] M. Lang, C. Trautmann, M. Toulemonde, D. Rodríguez, and Z. Wang, Nanoscale manipulation of the properties of solids at high pressure with relativistic heavy ions, Nat. Mater. **8**, 793 (2009).

[41] M. Lang, J. Lian, J. Zhang, F. Zhang, W. J. Weber, C. Trautmann, and R. C. Ewing, Single-ion tracks in $Gd_2Zr_{2-x}Ti_3O_7$ pyrochlores irradiated with swift heavy ions, Phys. Rev. B **79**, 224105 (2009).

[42] J. Liu, U. A. Glasmacher, M. Lang, C. Trautmann, K.-O. Voss, R. Neumann, G. A. Wagner, and R. Miletich, Raman spectroscopy of apatite irradiated with swift heavy ions with and without simultaneous exertion of high pressure, Appl. Phys. A **91**, 17 (2008).

[43] M. Lang, F. Zhang, J. Lian, C. Trautmann, R. Neumann, and R. C. Ewing, Combined high pressure and heavy-ion irradiation: A novel approach, J. Synchrotron Rad. **16**, 773 (2009).

[44] U. A. Glasmacher, M. Lang, H. Keppler, F. Langenhorst, R. Neumann, D. Schardt, C. Trautmann, and G. A. Wagner, Phase transitions in solids stimulated by simultaneous exposure to high pressure and relativistic heavy ions, Phys. Rev. Lett. **96**, 195701 (2006).

[45] M. Lang, F. Zhang, J. Lian, C. Trautmann, R. Neumann, and R. C. Ewing, Irradiation-induced stabilization of zircon ($ZrSiO_4$) at high pressure, Earth Planet. Sci. Lett. **269**, 291 (2008).

[46] M. Lang, F. Zhang, J. Zhang, J. Wang, J. Lian, W. J. Weber, B. Schuster, C. Trautmann, R. Neumann, and R. C. Ewing, Review of $A_2B_2O_7$ pyrochlore response to irradiation and pressure, Nucl. Instrum. Methods Phys. Res. B **268**, 2951 (2010).

[47] S. Park, C. L. Tracy, F. Zhang, C. Park, C. Trautmann, S. N. Tkachev, M. Lang, W. L. Mao, and R. C. Ewing, Radiation-induced disorder in compressed lanthanide zirconates, Phys. Chem. Chem. Phys. **20**, 6187 (2018).

[48] B. Schuster, F. Fujara, B. Merk, R. Neumann, T. Seidl, and C. Trautmann, Response behavior of $ZrO_2$ under swift heavy ion irradiation with and without external pressure Nucl. Instrum. Methods Phys. Res. B **277**, 45 (2012).

[49] J. F. Ziegler and J. P. Biersack, The stopping and range of ions in matter, in *Treatise on Heavy-Ion Science*, edited by D. A. Bromley (Springer, Boston, MA, 1985), Vol. 6, pp. 93–129.

[50] Atima stopping power database: https://www.isotopea.com/webatima/

[51] F. Ballarini, *et al.*, The FLUKA code: Overview and new developments, EPJ Nucl. Sci. Technol. **10**, 16 (2024).

[52] A. Stolic, Z. Rogic Miladinovic, M. Krstic, G. Stamboliev, V. Petrovic, and E. Suljovrujic, Radiation-induced synthesis of polymer networks based on thermoresponsive ethylene glycol propylene glycol monomers, Gels **11**, 488 (2025).

[53] J. Liang, L. Bayarjargal, I. Tzifas, R. Belikov, L. Wedek, C. Schröck, D. Merges, K.-O. Voss, P. Simon, C. Trautmann, M. E. Toimil-Molares, and B. Winkler, Structural and optical responses of molecular solids to swift heavy ion irradiation under high pressures, Phys. Chem. Chem. Phys. **28**, 7835 (2026).

[54] X. Wang and X. Liu, High pressure: A feasible tool for the synthesis of unprecedented inorganic compounds, Inorg. Chem. Front. **7**, 2890 (2020).

[55] M. E. Toimil-Molares, Characterization and properties of micro- and nanowires of controlled size, composition, and geometry fabricated by electrodeposition and ion-track technology, Beilstein J. Nanotechnol. **3**, 860 (2012).

[56] C. Schröck, I. Tzifas, K.-O. Voss, M. F. P. Wagner, C. Trautmann, L. Bayarjargal, D. Spahr, B. Winkler, and M. E. Toimil-Molares, Influence of diameter on high-pressure induced phase transitions in bismuth nanowire networks, Phys. Rev. B **112**, 014111 (2025).

[57] A. San-Miguel, Nanomaterials under high-pressure, Chem. Soc. Rev. **35**, 876 (2006).

[58] F. Bai, K. Bian, X. Huang, Z. Wang, and H. Fan, Pressure induced nanoparticle phase behavior, property, and applications, Chem. Rev. **119**, 7673 (2019).

[59] https://www.gsi.de/work/organisation/wissenschaftliche_gremien/pac/mat_pac